Characterisation of the oxidation and creep behaviour of novel Mo-Si-Ti alloys

Susanne Obert, Alexander Kauffmann*, and Martin Heilmaier

Karlsruhe Institute of Technology (KIT), Institute for Applied Materials (IAM-WK), Engelbert-Arnold-Straße 4, 76131 Karlsruhe, Germany

* corr. author: alexander.kauffmann@kit.edu; +49 721 608 42 346

Abstract

The oxidation and creep behaviour of novel eutectic-eutectoid Mo-Si-Ti alloys were studied and compared to previously investigated entirely eutectic Mo-20Si-52.8Ti (at%) and eutectoid Mo-21Si-34Ti reference alloys [Schliephake et al. in Intermetallics 104 (2019) 133-142]. While the latter reference alloys showed either outstanding oxidation behaviour in the temperature range of 800 to 1200 °C (eutectic alloy) or reasonable creep resistance (eutectoid alloy), a combination of both was successfully achieved in a Ti-rich alloy variant (Mo-21Si-43.4Ti). The ubiquitous catastrophic oxidation ("pesting") of Mo-based alloys at 800 °C is suppressed in this alloy and reasonable oxidation resistance at higher temperatures is observed. For the first time, the unexpected oxidation resistance of the alloys exhibiting eutectic volume fractions of more than 50 vol% is rationalised by a systematic deconvolution of mass gain by scale formation and mass loss by evaporation of volatile species. Furthermore, creep is revealed to be based on similar creep mechanisms throughout the alloy series. Therefore, the observed improvement in creep resistance of the pesting-resistant Ti-rich alloy variant over the eutectic alloy is attributed to the decreasing homologous temperature when testing both at 1200 °C.

1. Introduction

Many attempts have been made by international researchers with the purpose of optimising the Mo-Si based alloy system in order to provide alternatives to Ni-based superalloys for high temperature applications. Most attention was paid to three-phase Mo-Si-B alloys which show very promising creep performance and satisfactory oxidation behaviour in the temperature regime of 1000 to 1200 °C [1-3]. However, they all suffer from the pesting phenomenon at temperatures below 1000 °C [4] which excludes them for wide industrial applications. Additionally, they possess significantly higher densities in the range of 9.5 g/cm^3 [5] compared to commercially used Ni-based superalloys. This drawback was successfully alleviated by macro-alloying with Ti reducing the density to 7.7 g/cm^3 [6, 7]. However, inadequate oxidation resistance at intermediate temperatures below 1000 °C is still present in these alloys [6]. The development of two-phase eutectic or eutectoid Mo-Si-Ti alloys in recent research work by Schliephake et al. [8] shows great potential in this respect. The novel eutectic and eutectoid two-phase, fine-scaled Mo-Si-Ti alloys with comparably low density of 6 to 7 g/cm^3 have shown to be either oxidation-resistant in the entire temperature range or sufficiently creep-resistant. The binary eutectic Mo-20Si-52.8Ti alloy consisting of Mo_{SS} and $(Ti,Mo)_5Si_3$ lamellae possesses outstanding oxidation

behaviour, namely insignificant and constant mass change subsequent to an initial parabolic oxidation behaviour at 1100 and 1200 °C as well as absence of any pesting-like behaviour at 800 °C. This unexpected oxidation resistance at 800 °C has been attributed to the formation of a mixed SiO_2-TiO_2 oxide scale [8]. In contrast, the eutectoid alloy Mo-21Si-34Ti comprising fine-structured Mo_{SS} and $(Mo,Ti)_5Si_3$ lamellae exhibits pesting behaviour at 800 °C, but reasonable creep resistance by means of one order of magnitude lower minimum creep rate compared to the eutectic alloy.

In order to achieve both, oxidation and creep resistance, in a single alloy, we suggest to synthesise a eutectic-eutectoid microstructure in the present study. The former addition of B [9-12] is claimed to be redundant as it is believed that the fine-scaled eutectic and eutectoid microstructures enable fast surface diffusion paths and, thus, will lead to rapid passivation by oxide scale formation.

2. Experimental

The alloys presented in this paper were arc-melted using high-purity bulk elements Mo, Ti and Si with purities 99.95, 99.8 and 99.99 %, respectively, in an Edmund Bühler GmbH AM/0,5 Arc Melter equipped with a water-cooled, button-shaped Cu crucible. Arc melting was conducted under Ar atmosphere at 600 hPa which was cleaned from O residuals by pre-melting a Zr lump. Prior to melting, the chamber was iteratively pumped and flooded with Ar before evacuating to 10^{-4} mbar. To guarantee homogeneity, the melting procedure was repeated by turning over the button and re-melting it for at least five times. The weight loss due to melting was confirmed to be below 0.5 wt%. The final shape of the ingots was achieved by re-melting in a nugget-shaped Cu crucible. Additional heat treatments were applied for specific alloys to complete the solid phase decomposition of $(Mo,Ti)_3Si$. These heat treatments were conducted in a Gero tube furnace (HRTH sinter furnace) at 1300 °C for 200 h under Ar atmosphere.

N and O impurities were determined by hot gas carrier extraction on a Leco TC500 device in order to determine. The N content was found to be below 0.004 at% and the O content in the order of 0.1 at% in all investigated alloys. The density was verified at room temperature by applying the Archimedes principle. The solidus temperature of the alloys and the Si content in Mo_{SS} were calculated by using the thermodynamic PANDAT software package (version of 2018) in conjunction with the commercially available database (PanMo2018a).

Oxidation and creep samples were manufactured by electrical discharge machining and prepared according to the planned testing.

Cyclic oxidation experiments were conducted in static laboratory air at 800, 1100 and 1200 °C in muffle furnaces provided by Gero and Nabertherm. The sample geometry was (5 x 5 x 4) mm^3. Prior to oxidation testing, the samples were ground to SiC grit P2500 to ensure appropriate surface finish. Mass change was determined after each cycle at room temperature utilising a Sartorius balance at an accuracy of 1 µg. The total test duration of the cyclic oxidation experiments was 100 h. The oxidation samples

were maintained in ceramic Al_2O_3 baskets throughout the entire testing but were flipped after each cycle. Isothermal oxidation experiments were carried out under synthetic air and Ar mixture with a ratio of 3:2 and flow rates of 30 ml/min and 20 ml/min, respectively, using a thermogravimetric analyser STA449 by Netzsch for continuous monitoring of the mass change. The oxidation samples were placed in Al_2O_3 baskets as well.

Compressive creep tests at constant true stress were performed under vacuum between 1050 and 1316 °C at true stresses ranging from 50 to 300 MPa. The universal testing machine was provided by Zwick and was equipped with a vacuum furnace by Maytec. The load was applied to the compression samples via punches which were made of SiC. The ground front faces of the samples were lubricated by means of hexagonal BN.

Scanning electron microscopy (SEM) was conducted using backscatter electron contrast (BSE) in a LEO EVO 50 SEM by Zeiss equipped with an energy dispersive X-ray spectroscopy (EDX) system. EDX was used to characterise the obtained microstructures and oxide morphology of the oxidation samples. Volume fractions were determined by manually denoting the various microstructural regions using the image processing software Corel Photo-Paint and subsequent determination of areal fraction in the software ImageJ. The equivalence of areal fraction and volume fraction was based on the assumed isometry and isotropy of the investigated microstructures. Determination of the interface density P was conducted by means of evaluation of binarised BSE images with the linear intercept method. The morphology of the oxide scales was analysed by means of cluster analysis of binarised greyscale BSE images. All 8-connected pixels were detected in the binary images, combined to regions of pixels, and finally each region was colour-coded by utilising a self-made Matlab script.

X-ray diffraction (XRD) measurements were performed using a D2 phaser device of Bruker in Bragg-Brentano geometry operating with Cu K_α radiation. The Cu tube was operated at 30 kV and 10 mA, and the according radiation was filtered by means of Ni foil. The radiation was detected using a LynxEye line detector at a step size of 0.01 ° in 2Θ with an accumulated time of 384 s per step. Lattice parameters were determined by evaluating the corresponding peak positions with a Nelson-Riley approach [13].

3. Results and discussion

3.1. Alloy strategy and resulting microstructure

The alloy design strategy focuses on the development of novel Mo-Si-Ti alloys with tailored eutectic-eutectoid microstructures comprising minor volume fractions of primary solidified Mo_{SS}. The starting points were the former investigated eutectic Mo-20Si-52.8Ti (green symbol in the relevant section of the liquidus projection of the ternary Mo-Si-Ti system, Fig. 1) and eutectoid Mo-21Si-34Ti (blue symbol) reference alloys in Ref. [8]. Two novel alloys within the chemical composition range framed by these two reference alloys were examined: (a) the Ti-rich alloy A Mo-21Si-43.4Ti (red symbol) being

closer to the composition of the eutectic alloy and the Ti-lean alloy B Mo-21Si-38.7Ti (black symbol) being near to the eutectoid alloy.

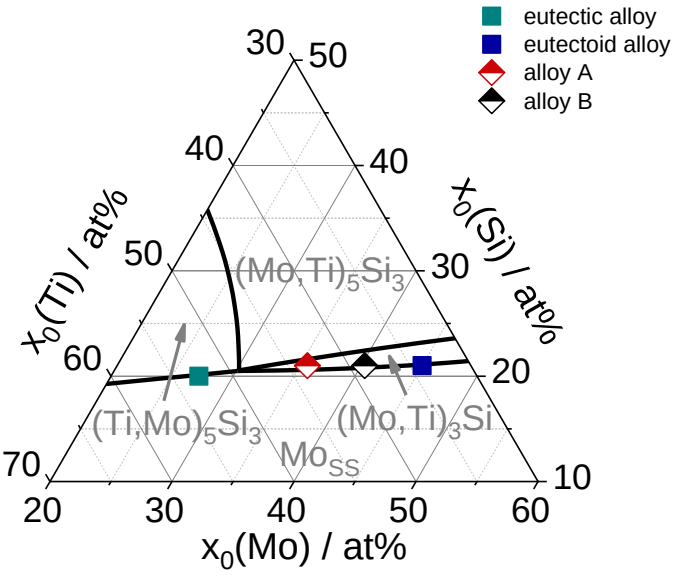

Fig. 1 Section of the liquidus projection of the ternary Mo-Si-Ti system highlighting the investigated alloys (coloured symbols) and the primary solidifying phases (grey labels).

Table 1 summarises the details of the chemical compositions of the investigated alloys and their microstructural characteristics. Note that alloy A does not require an additional heat-treatment since $(Mo,Ti)_3Si$ decomposes completely during processing, as will be shown in the further course of this article, and is therefore characterised in the as-cast sate (designated ac in what follows). In contrast, alloy B contains $(Mo,Ti)_3Si$ in the as-cast state, hence an additional heat-treatment (ht) at 1300 °C for 200 h under Ar atmosphere is applied to achieve complete eutectoid decomposition.

Table 1 Summary of chemical and microstructural data of the investigated alloys: nominal compositions x_i, volume fraction of primary solidified Mo_{SS} $v^{Mo_{SS}{}^{primary}}$, volume fractions of $(Mo,Ti)_3Si$ $v^{(Mo,Ti)_3Si}$, eutectoid and eutectic regions $v^{eutectoid}$ and $v^{eutectic}$, phase boundary fraction P and density ρ. * in the heat-treated condition.

#	i	x_i / at%	$v^{Mo_{SS}{}^{primary}}$ / vol%	$v^{(Mo,Ti)_3Si}$ / vol%	$v^{eutectoid}$ / vol%	$v^{eutectic}$ / vol%	P / µm^{-1}	ρ / g/cm^3
A	Mo	35.6	3.1 ± 1.2	-	46.7 ± 6.1	50.2 ± 6.3	0.6 ± 0.1	6.49
	Si	21						
	Ti	43.4						
B	Mo	40.3	6.8 ± 1.7	13.5 ± 4.0	36.7 ± 2.0	45.4 ± 3.5	1.0 ± 0.1*	6.84
	Si	21						
	Ti	38.7						

The corresponding microstructures of the investigated alloys including the eutectic and eutectoid reference alloys are shown in the BSE micrographs in Fig. 2. The reference alloys comprise fully lamellar eutectic and eutectoid microstructures, respectively, whereas the intermediate alloys are characterised by a combination of both. The intermediate alloys are differently fine-scaled due to the additionally applied heat-treatment of alloy B, as confirmed by the determination of the phase boundary density *P* (see Table 1). In the present study it is not possible to experimentally determine the chemical composition of the silicide phase of the eutectic or eutectoid by EDX due to its fine-scaled microstructure. Nonetheless, it is assumed that the eutectoid is composed of Mo_{SS} and $(Mo,Ti)_5Si_3$ lamella as z-contrast of the respective silicide lamella reveals a brighter grey level compared to the silicide lamella of the eutectic. The contrast difference is mostly attributed to the different contents of Mo (brighter) and Ti (darker) which occupy the respective lattice site(s) in either $(Mo,Ti)_5Si_3$ and $(Ti,Mo)_5Si_3$ while the Si remains virtually unaffected by the actual type of silicide. Nevertheless, unambiguous evidence for the crystal structure of the respective 5-3 silicide cannot be provided by this kind of images.

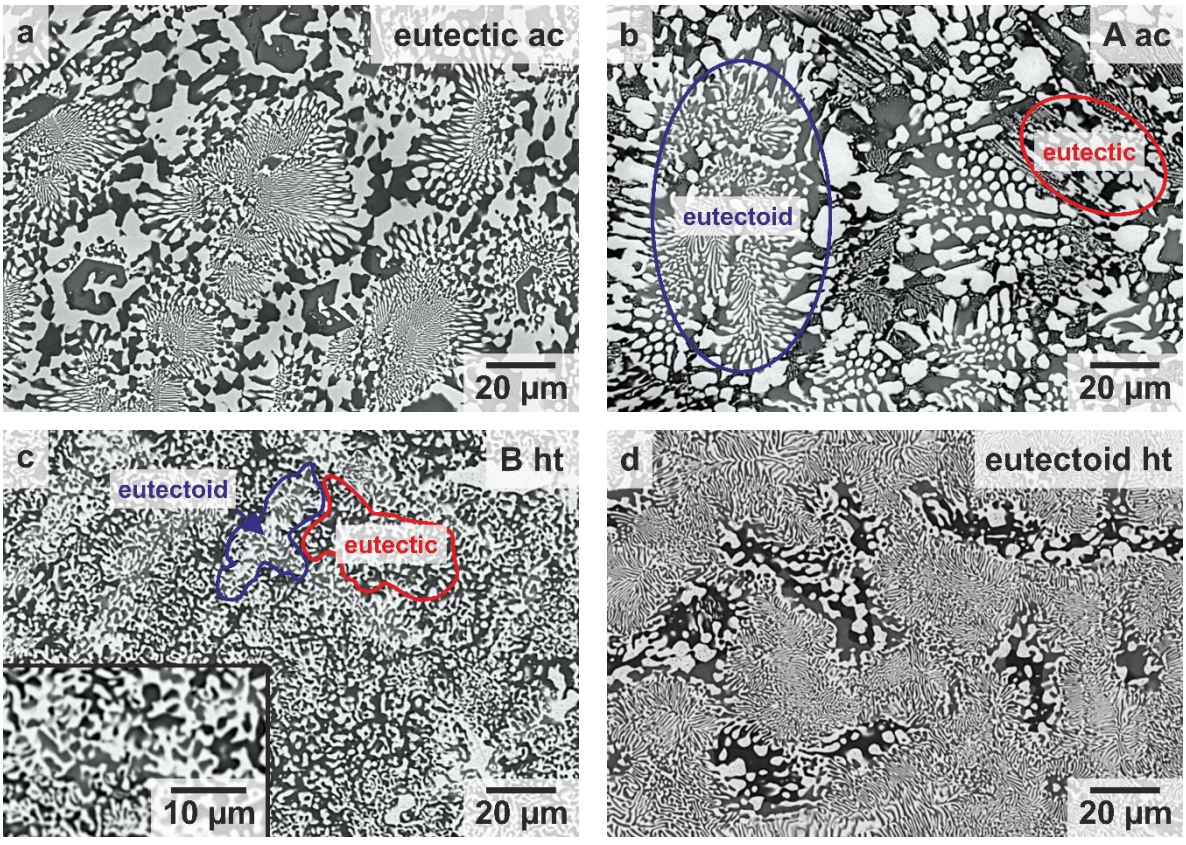

Fig. 2 BSE micrographs of the microstructures of the as-cast eutectic reference alloy (a), alloy A as-cast (b), alloy B heat-treated at 1300 °C for 200 h (c) and the eutectoid reference alloy heat-treated at 1300 °C for 200 h (d). The seen phases/-regions are Mo_{SS} (bright), $(Mo,Ti)_5Si_3$ (light grey), $(Ti,Mo)_5Si_3$ (dark grey), lamellar eutectic (red highlighted) and lamellar eutectoid (blue highlighted) microstructures.

To further address the determination of the present phases, XRD analyses were performed in the as-cast state of alloy A and the heat-treated condition of alloy B. The presence of Mo_{SS}, and both, $(Ti,Mo)_5Si_3$ and $(Mo,Ti)_5Si_3$ could be confirmed (see Suppl. 1).

In addition, the lattice parameters of Mo_{SS} in the investigated alloys were determined and compared to the lattice parameters of binary bcc Mo-Ti solid solutions reported in literature [14] as shown in Fig. 3. This comparison allows for a determination of the phase specific Ti content in the bcc solid solution when the Si contribution to the lattice parameter is neglected and considered to be similar among the alloy series. These considerations are assumed to be appropriate as Sturm et al. have shown that the lattice parameter of Mo-Si solid solutions only decreased by 0.2 % when 3.34 at% Si were added [15]. Furthermore, thermodynamic calculations predict a maximum Si content in Mo_{SS} of 4 at% in all investigated alloys when the solidification process starts. By taking the applied manufacturing route of arc melting with subsequent heat treatment in some cases into account, it is likely that present Mo_{SS} comprises Si in the order of 2 to 4 at% (4 at% in case of arc-melted, fast-cooled specimen and lower for heat-treated, slowly-cooled samples). The phase specific composition – especially the one of the bcc solid solution – is a crucial parameter for the assessment of oxidation behaviour in the further course of this article but is typically difficult to be reliably determined due to the rather fine scale morphology of the phases. Furthermore, local TEM investigations of the Ti content in the Mo_{SS} lamellae in the eutectic or eutectoid might certainly be more accurate but due to the small investigated volume, fluctuations among different regions, namely primarily solidified Mo_{SS}, lamellae adjacent to and $(Mo,Ti)_5Si_3$ vs. lamellae adjacent to $(Ti,Mo)_5Si_3$, remain difficult to be addressed. Therefore, the here presented evaluation only holds true for the average Ti content in Mo_{SS} including the overall microstructure, especially in the intermediate eutectic-eutectoid alloys A and B, including both, eutectic and eutectoid regions, which possibly possess different Ti contents on local scale. These differences have to be assessed in future work. The lattice parameters of Mo_{SS} in the reference alloys frame the intermediate eutectic-eutectoid alloys well. In general, a consistently lower Ti content in Mo_{SS} in contrast to the nominal Ti content could be determined in all investigated alloys. This reveals that Ti is significantly solved in the silicide phases. The eutectic alloy possesses the largest Ti-concentration in Mo_{SS} at 45 at%, while the eutectoid alloy represents the lower limit with only 17 at% Ti. The intermediate alloys comprise average, global Ti contents of around 35 at% (alloy A) and 25 at% (alloy B). However, an estimated inaccuracy of the lattice parameters of maximum 0.001 Å leads to an uncertainty in the determination of the Ti content of approximately 1.4 at% in the eutectic alloy and more than 5 at% in the eutectoid alloy.

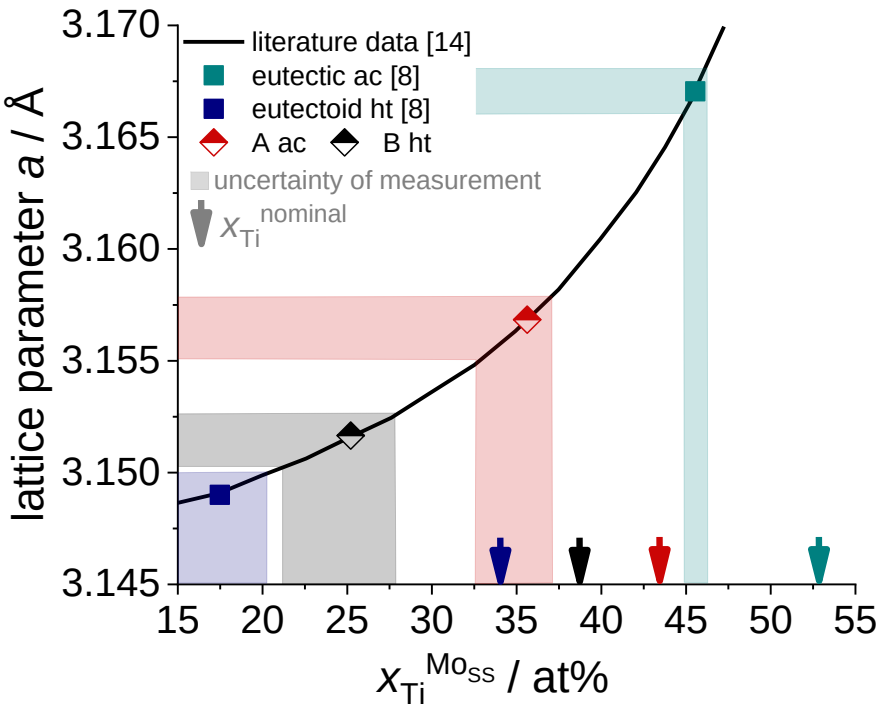

Fig. 3 Experimentally determined lattice parameters of Mo_{SS} in the investigated alloys compared to the lattice parameters of binary Mo-Ti solid solution as a function of Ti content reported in Ref. [14] and compared to the eutectic and eutectoid reference alloys evaluated in Ref. [8]. The semi-transparent regions indicate the estimated uncertainty of the lattice parameters and its conversion to the Ti content. Arrows at the abscissa indicate the nominal Ti contents of the alloys.

3.2. Oxidation behaviour

All aforementioned alloys including the eutectic and eutectoid reference alloys were subjected to isothermal and cyclic oxidation tests at 800, 1100 and 1200 °C. The specific weight changes, at least three samples in each case, in dependence of test duration during cyclic oxidation tests at 800 and 1200 °C are plotted in Fig. 4. The results gained at 1100 °C are included in supplementary material to this article (Suppl. 2) as similar oxidation behaviour to 1200 °C is observed. As 800 °C is the critical temperature where pesting occurs, the corresponding isothermal oxidation tests of alloy A and B are included as well. The following results can be concluded from these experiments: (i) The previously reported results on the oxidation behaviour of the eutectic and eutectoid reference alloys by Schliephake et al. [8] are very well reproduced (see Suppl. 3). The eutectic alloy exhibits low mass changes in the entire temperature range. In contrast, the eutectoid alloy shows catastrophic oxidation at 800 °C, and slightly larger mass changes compared to the eutectic alloy at higher temperatures with significant scatter between different samples. Nevertheless, the mass changes saturate after some duration of exposure. (ii) Both alloys with intermediate Ti contents (A and B) exhibit different oxidation behaviour but with significant similarities to the reference alloys. While alloy B suffers from pesting at 800 °C like the eutectoid alloy and conventional Mo-Si based alloys [6, 16], alloy A shows similar adequate oxidation resistance like the eutectic alloy at 800 °C, but with slightly larger weight change after 100 h by means of (-2.0 ± 0.7) g/cm^2 compared to (0.1 ± 0.1) g/cm^2 in the eutectic alloy. At 1200 °C, all alloys show comparable adequate oxidation behaviour with reasonable mass changes in the range of

(3.1 ± 0.1) g/cm^2 (eutectic), (-14.8 ± 12.3) g/cm^2 (eutectoid), (2.7 ± 1.9) g/cm^2 (A), and (-13.2 ± 15.9) g/cm^2 (B). However, some scatter in mass change is present at higher temperatures, which is attributed to local inhomogeneity of the as-cast and heat-treated microstructure, respectively.

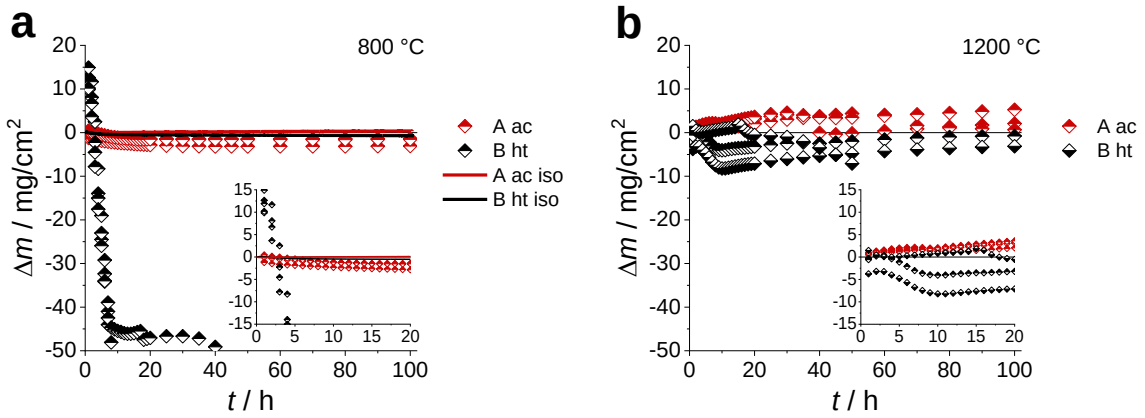

Fig. 4 Specific weight change as a function of time during cyclic and isothermal oxidation for the investigated alloys A and B at 800 °C (a), and for cyclic oxidation at 1200 °C (b).

Additionally, isothermal oxidation tests at 800 °C were performed revealing similar trends in isothermal mass change for all investigated alloys (see Suppl. 4 for isotherms at 1100 and 1200 °C of all investigated alloys). It was shown that (i) at 800 °C no pesting occurs, even not in alloy B which is contrary to the cyclic oxidation experiments and most probably due to the absence of thermally induced loading provoking oxide scale cracking and the Ar to synthetic air ratio. (ii) Slightly higher mass gain in alloy A and B in the order of 5 g/cm^2 (1100 °C) and 20 mg/cm^2 (1200 °C) at temperatures above 800 °C which is most likely to be caused by the flowing synthetic air leading to higher O activity at the surface.

SEM analyses of cross sections subsequent to cyclic oxidation after exposure times of 1 h and 100 h were performed in order to investigate the oxide scale morphology. Representative BSE micrographs of oxidised samples of alloy A at 800 °C are depicted in Fig. 5. The initial oxidation during the first hour of exposure at 800 °C is characterised by the formation of an outer TiO_2-rich oxide scale with locally minor adherence, as cracking at the oxide scale substrate interface is observed (see Fig. 5a) and internal oxidation which occurs preferentially in the eutectoid regions close to the surface (see Fig. 5a and b). This confirms the strikingly different oxidation behaviour of the eutectic and eutectoid at 800 °C. The former Mo_{SS} lamellae or primary solidified Mo_{SS} either oxidise internally to (Ti,Si)-oxide guiding the oxidation attack towards the internal of the substrate, or if located at the surface oxidise to TiO_2 which covers the surface while enabling O inward diffusion. This is remarkable as primary solidified Mo_{SS} might directly oxidise to MoO_3 leaving pores behind upon exposure to air. In this study, it is assumed that formed MoO_3 is evaporating quickly in alloy A, as some pores are enclosed in the internal oxidation zone (see Fig. 5a). Nevertheless, the mass loss is probably compensated by the simultaneous rapid formation of TiO_2 which is enabled by the rapid outward diffusion of Ti. Therefore, the suppression of pesting in alloy A is attributed to the high average Ti content of Mo_{SS} lamellae within the eutectic and

eutectoid regions being approximately 35 at%. However, due to the different oxidation behaviour of the eutectic and eutectoid regions, it is likely that the oxidation-resistant eutectic region comprises a higher local Ti content in Mo_{SS}. The oxidation-resistant eutectic alloy reveals a Ti content in Mo_{SS} of 45 at%. In contrast to both, the eutectoid alloy suffering from pesting contains only 17 at% Ti in Mo_{SS}. After 100 h, the outer TiO_2 oxide scale measures an average thickness of (4 ± 2) µm, with an internal oxidation zone measuring (23 ± 10) µm in thickness in alloy A.

Additionally, pre-oxidation experiments of alloy A at 1100 °C for 10 h in laboratory air lead to the formation of a mixed SiO_2-TiO_2 oxide scale with an average thickness of less than 10 µm. It enables the substrate to withstand cyclic oxidation experiments at 800 °C for 100 h without significant internal oxidation, as was observed for non-pre-oxidised samples. Furthermore, the adequate specific weight change is in the range of less than 3 mg/cm^2 (see Fig. 5c). This might be due to the dense oxide scales formed at 1100 °C after 10 h hindering further inward O diffusion at 800 °C and therefore preventing internal oxidation. Furthermore, the oxide scale (originally formed at 1100 °C after 10 h) growth at 800 °C is retarded compared to the observations made for the cyclic oxidised samples at 1100 °C for 100 h. Under isothermal conditions at 800 °C alloy A reveals a thin SiO_2-TiO_2 mixed oxide scale with a thickness of less than 5 µm in average without any indications of internal oxidation as shown in Fig. 5d. The thin and continuous oxides scale might be attributed to the absence of thermo-cycling induced cracking and is in well agreement with the negligible mass change detected.

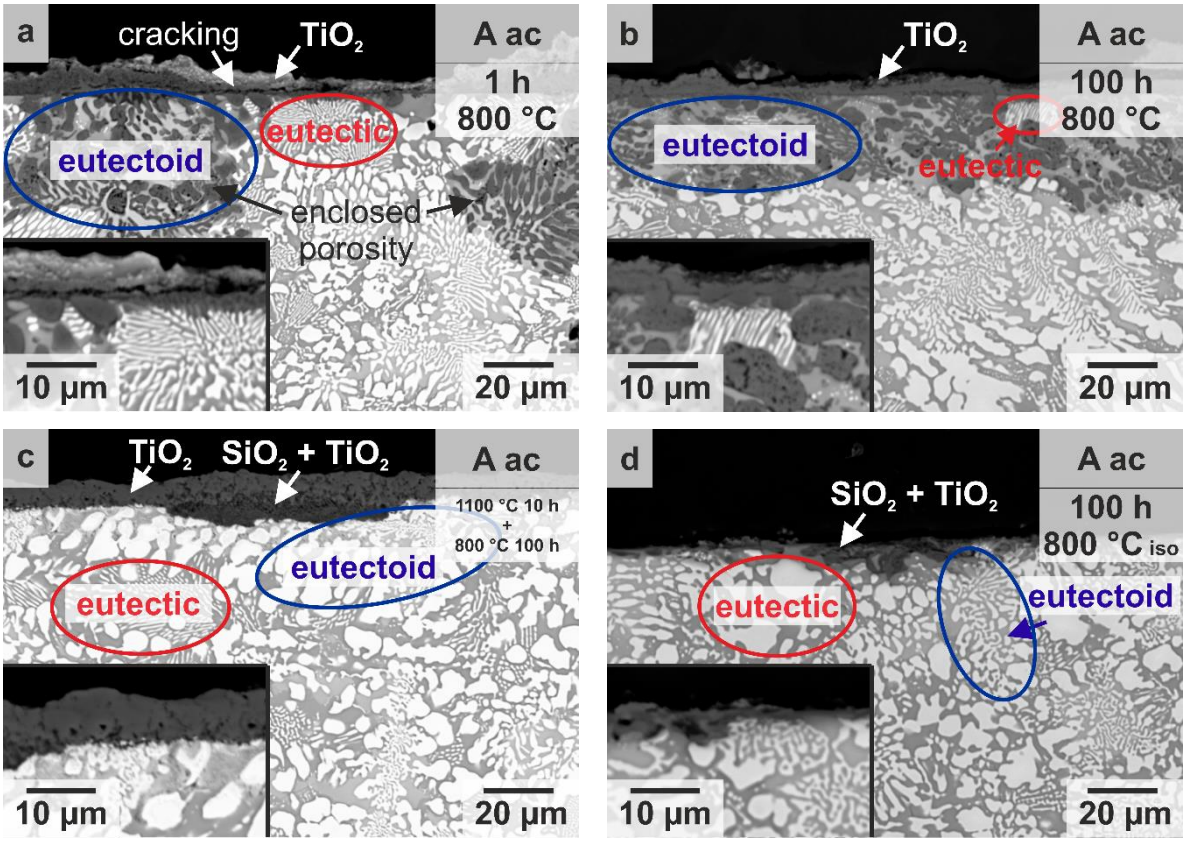

Fig. 5 Representative BSE micrographs of the cyclic oxidised samples at 800 °C after 1 h (a) and 100 h (b) of alloy A; pre-oxidised sample (1100 °C/10 h/air) of alloy A after cyclic oxidation at 800 °C for 100 h (c) and after isothermal oxidation at 800 °C for 100 h (d).

In comparison to the oxidation behaviour of the investigated alloy A, the eutectic reference alloy exhibits a very thin, continuous mixed SiO_2-TiO_2 oxide scale after 1 h exposure time at 800 °C which grows to a thickness of only (5 ± 1) µm in average after 100 h without any internal oxidation (see Suppl. 5a and b). These results confirm the reproducibility of the oxidation behaviour of the eutectic alloy previously presented in Ref. [8].

In contrast, the Ti-lean alloy B suffers from pesting under cyclic testing conditions. Due to the significant oxidation attack, cracking in the oxide scale and the internally oxidised substrate even after 1 h, a difference between the eutectic and eutectoid regions in oxidation behaviour could not be observed, as shown in Fig. 6a. Although pesting is observed like in the eutectoid reference alloy, it is less severe, as mass losses stabilise after approximately 20 h and only partial material disintegration with local spalling is observed (see Suppl. 5c and d). It seems that alloy B might not be oxidation-resistant itself or that the eutectic regions were not able to protect it from pesting. The main reasons might be: (i) The Ti content in Mo_{SS} is only about 25 at%, being remarkably lower than that of the eutectic alloy and alloy A, which might be insufficient to enable TiO_2 formation and to reduce the probability of MoO_3 formation. Thus, it is assumed that there exists a Ti-threshold content for Mo_{SS} which determines whether pesting occurs, or not. (ii) The volume fraction of the eutectic microstructure is in the range of (50 ± 6) vol% in alloy A in contrast to (45 ± 3) vol% in alloy B. The volume fraction and distribution of the eutectic is likely to play a decisive role when suppressing pesting as in alloy A an almost binary eutectic network is present which enables quick coverage of the surface accompanied with bridging eutectoid regions. Thereby, in alloy A locally present primary solidified Mo_{SS} does not disturb oxide scale formation at the surface but oxidises internally itself. It is assumed that due to the low Ti content in Mo_{SS} and the higher volume fraction of eutectoid microstructure in alloy B, MoO_3 formation was dominant leading to pesting. The aforementioned striking difference in oxidation behaviour at 800 °C between cycylic and isothermal oxidation testing is suppported by Fig. 6b and c. It is revealed that a thin, continuous and especially crack-free mixed SiO_2-TiO_2 oxide scale forms under isothermal conditions preventing catastrophic oxidation.

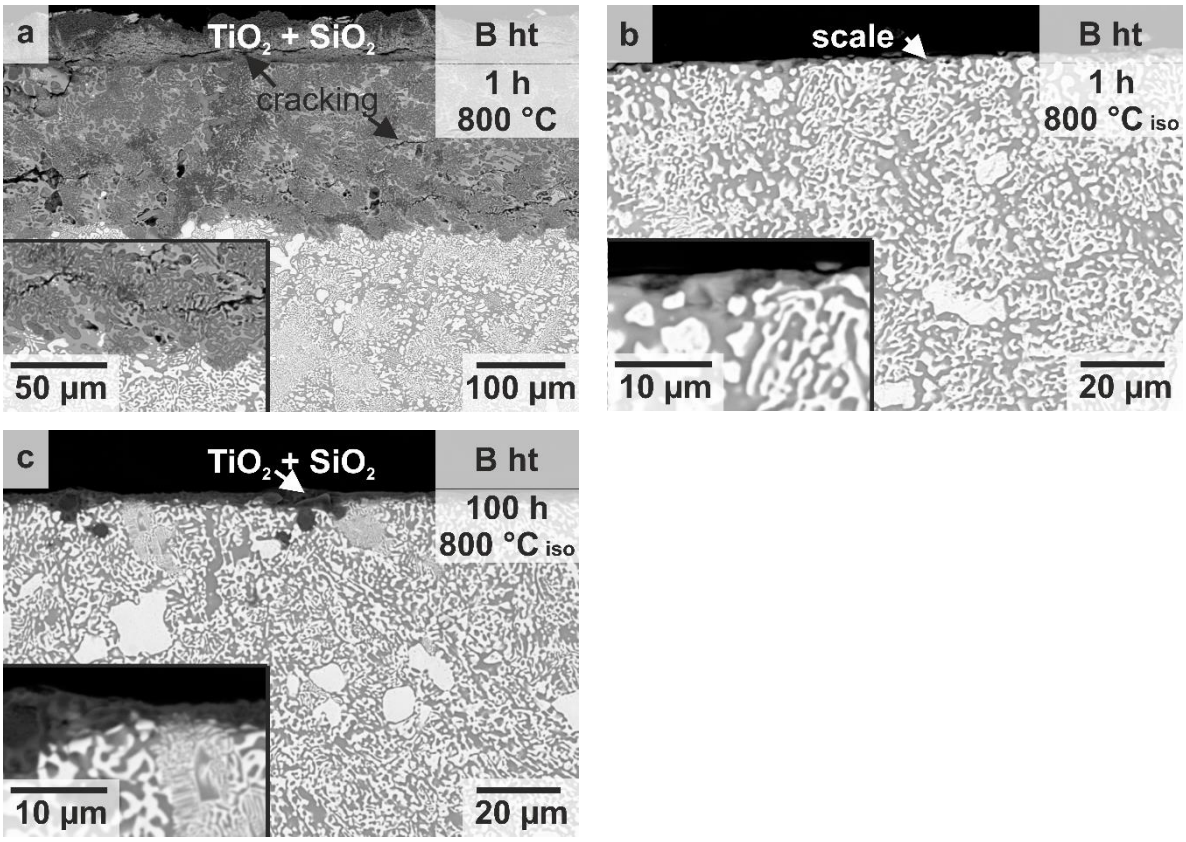

Fig. 6 Representative BSE micrographs of alloy B after 1 h cyclic (a) and isothermal oxidation (b) at 800 °C and after 100 h isothermal oxidation at 800 °C.

237 At 1100 and 1200 °C, an outer TiO_2 oxide scale is formed with an underlying SiO_2-TiO_2 duplex scale
238 on all investigated intermediate alloys. Fig. 7 shows oxidised samples at 1200 °C; due to the similarity
239 of the oxide scale morphology, the cross sections at 1100 °C are omitted. This was also observed on the
240 eutectic and eutectoid reference alloys (see Suppl. 5e and f).

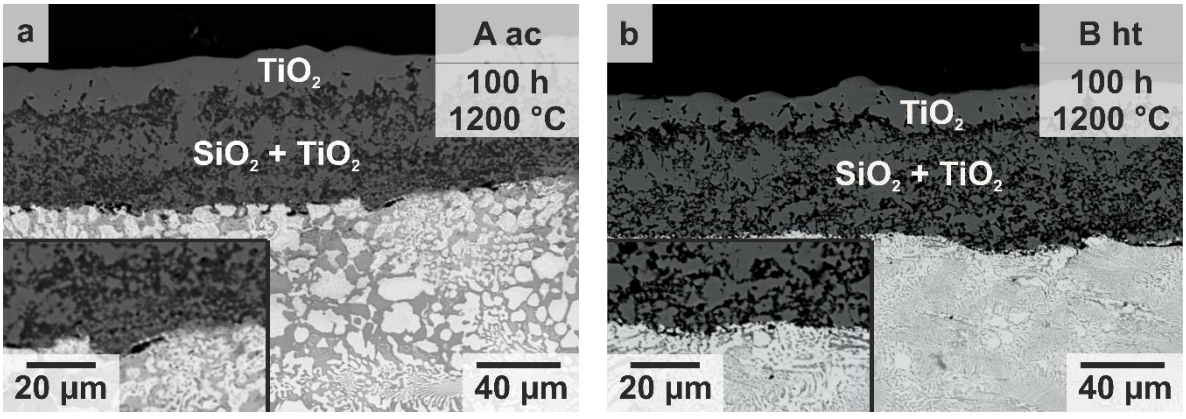

Fig. 7 Representative BSE micrographs of the cyclic oxidised samples at 1200 °C after 100 h of alloy A as-cast (a) and alloy B heat-treated (b).

241 The corresponding oxide scale evolution at 1200 °C is addressed by the oxide scale thickness and the
242 respective SiO_2 volume fraction in the SiO_2-TiO_2 duplex scale after 100 h in Fig. 8. A trend seems to be
243 present regarding the evolution of the absolute oxide scale thickness in dependence of the nominal Ti
244 content in the investigated alloys (see Fig. 8a). While the eutectic alloy possesses the thinnest oxide

scale with an absolute thickness of 50 µm in average (52.8 at% nominal Ti), the eutectoid alloy exhibits the thickest oxide scale with about 80 µm in thickness (34 at% nominal Ti). The intermediate alloys A and B range in between, namely 70 µm and 75 µm, respectively, pronouncing a trend towards increase in oxide scale thickness with decreasing nominal Ti content. This is somehow mirrored in the depth of the internal oxidation as well, which is increasing with decreasing nominal Ti content, namely from 10 µm in the eutectic alloy to approximately 55 µm in the eutectoid alloy. This trend might be supported by the eutectic volume fraction in the investigated alloys, which is continuously decreasing from almost 100 vol% in the eutectic alloy, to 50 vol% in alloy A to 45 vol% in alloy B and zero in the eutectoid alloy. These conclusions might be further correlated to the suppression of pesting at 800 °C, which is achieved in the Ti-rich alloy A and the eutectic reference alloy. When considering the volume fraction of SiO_2 in the SiO_2-TiO_2 duplex scale as depicted in Fig. 8 as well, it can be revealed that the SiO_2 volume fraction is in the same range for all investigated alloys, meaning 52 vol% (eutectic alloy), 48 vol% (alloy A), 43 vol% (alloy B) and 47 vol% (eutectoid alloy).

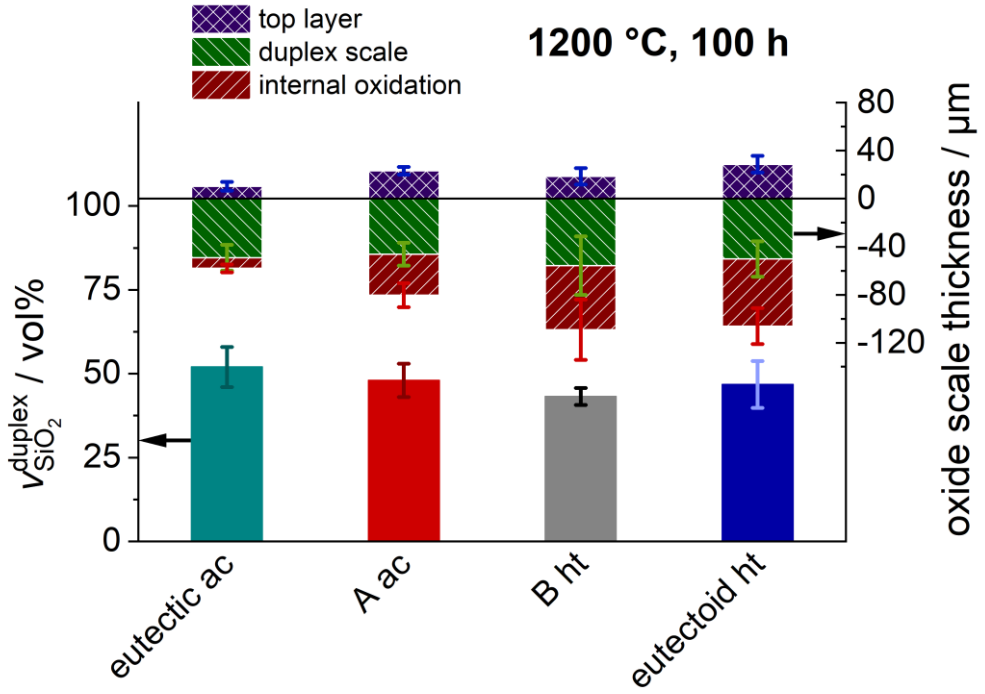

Fig. 8 Volume fraction of SiO_2 in the SiO_2-TiO_2 duplex scale on cyclic oxidation samples after 100 h at 1200 °C and the corresponding oxide scale thicknesses of the investigated alloys A, B and the reference alloys.

However, conclusions on the matrix forming oxide drawn from the results on the volume fraction of the respective oxides in the SiO_2-TiO_2 duplex scale have to be regarded with precautions. The determination of the matrix forming oxide is not trivial as the growth kinetics of the individual oxides, their interactions and mass loss due to evaporation play a crucial role. Therefore, the matrix forming oxide cannot be solely identified based on the volume fraction of the respective oxides. Especially, the evaluation of 2D micrographs does not provide any information on the 3D network structures of the SiO_2 and TiO_2 oxides, which is decisive for the determination of the matrix forming oxide. The representative BSE micrographs of the oxide scales formed on alloy A and alloy B at 1200 °C after 100 h shown in Fig. 7

might lead to the suggestion that SiO_2 could be the matrix forming oxide in the SiO_2-TiO_2 duplex scale as many SiO_2 regions seem to be connected. These apparent connections can be further assessed by pixel connectivity analysis as depicted in Fig. 9 for the eutectic reference alloy, the intermediate alloys A and B and the eutectoid reference alloy. Pixel clusters of TiO_2 correspond to cold colours (blue to green) and SiO_2 clusters to warm colours (red to yellow). In the eutectic reference alloy, several SiO_2 clusters are homogenously distributed within the duplex scale, however these are only laterally connected within regions of approximately 20 to 60 µm (see Fig. 9a). In contrast, the segmentation of TiO_2 reveals a penetrating network structure leading to the assumption that TiO_2 might be the matrix forming oxide. The same SiO_2 network structure within the duplex scale is observed in alloy A, where several SiO_2 clusters are present, though they do not penetrate the oxide scale in its full depth, as shown in Fig. 9b. Penetrating TiO_2 pathways are present, as well. This appearance is also observed in alloy B where the SiO_2 regions are mostly isolated horizontally, as depicted in Fig. 9c; whereas TiO_2 is revealed to form a continuous 2D network within large areal fractions of the SiO_2-TiO_2 duplex scale. Taking the eutectoid reference alloy into account (see Fig. 9d), it is revealed that all alloys, both reference alloys and the intermediate eutectic-eutectoid alloys mostly reveal a fine-structured, but discontinuous 2D SiO_2 network within the SiO_2-TiO_2 duplex scale including penetrating pathways of TiO_2 connecting the oxide surface with the substrate. Therefore, the significance of SiO_2 (as matrix forming oxide or high volume fraction) in the oxide scale, as highlighted in previous research on $Ti_5Si_{3\pm x}$ at 1000 °C [17], $(Mo,Ti)_5Si_3$ between 750 °C and 1300 °C [18, 19] and Mo-Si-B-Ti-Fe alloys at 1100 °C [20], might be less relevant in order to achieve reasonable oxidation resistance, since both intermediate alloys are reasonably oxidation-resistant at 1200 °C like both reference alloys even with locally penetrating TiO_2 pathways.

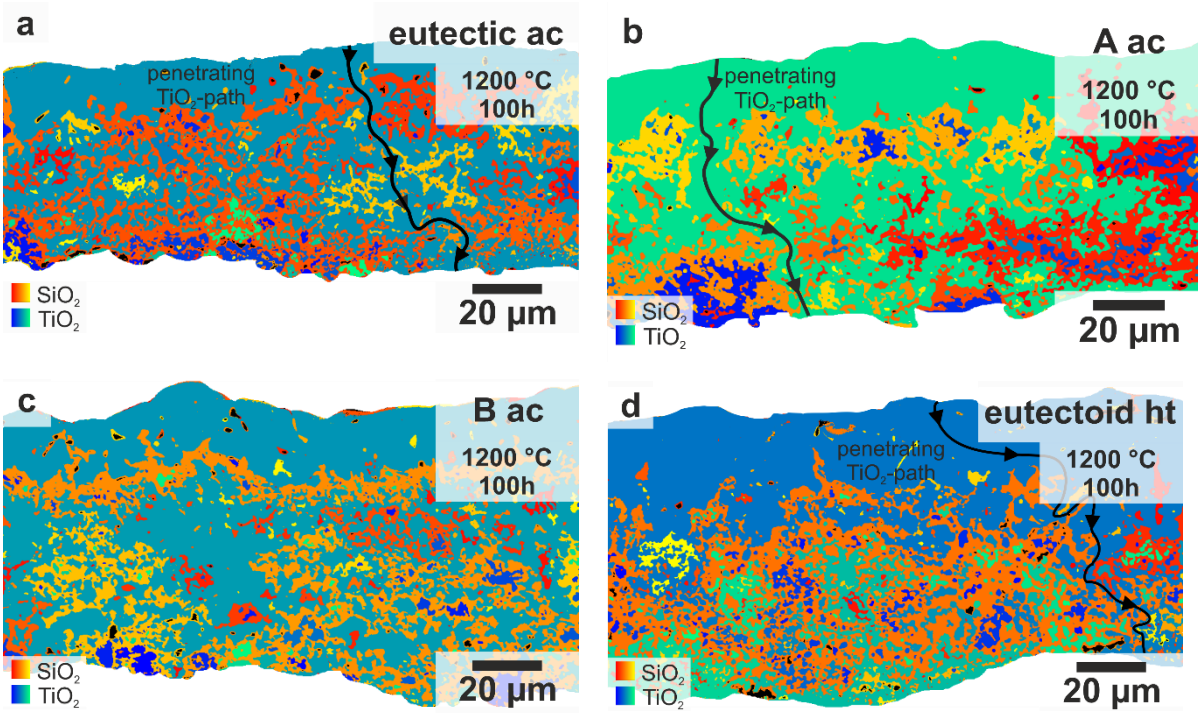

Fig. 9 Colour-coded images of the oxide scales formed on the eutectic reference alloy (a), alloy A (b), alloy B (c) and the eutectoid reference alloy (d) at 1200 °C after 100 h. SiO_2 is coloured in warm colours (red to yellow) and TiO_2 in cold (blue to green). Penetrating pathways in TiO_2 are highlighted as black, arrowed line.

Several conclusions can be drawn from the oxide scale thickness, the corresponding volume fraction of SiO_2 in the SiO_2-TiO_2 duplex scale as addressed in Fig. 8 and the oxide cluster analysis depicted in Fig. 9: (i) The probably expected correlation of less nominal Ti content in the alloy substrate leading to an increased volume fraction of SiO_2 in the SiO_2-TiO_2 duplex scale could not be observed. (ii) The absolute oxide scale thickness shows a continuously increasing trend with decreasing nominal Ti content. (iii) The SiO_2-TiO_2 duplex scale does not necessarily has to comprise an SiO_2 matrix in order to enable reasonable oxidation resistance at 1200 °C. This was proven by the presence of TiO_2 pathways penetrating the oxide scale from its surface to the interface with the alloy substrate. This trend might be extrapolated as a general result to 1100 and 800 °C, respectively. The penetrating pathways are especially observed in the intermediate alloys A and B, whereas the eutectoid alloy most likely possesses an SiO_2 matrix. Moreover, the eutectoid alloy reveals a rather high volume fraction of SiO_2, but the most severe internal oxidation. In contrast, the eutectic alloy comprises an internal corrosion zone of only 10 µm in depth with a comparable amount of SiO_2 in the SiO_2-TiO_2 duplex scale. These assumptions might hold true for the lower test temperatures as well. This is in contrast to the conclusions drawn in literature where SiO_2 is assumed to be the matrix forming oxide in order to achieve suitable oxidation resistance [17-20]. (iv) All alloys are comparably fine-structured as confirmed by the determination of the interface density. It can be concluded that the oxide scale formation, growth and morphology are dependent on the nominal chemical composition and are a function of the test temperature.

Unambiguously, 800 °C is the critical temperature and therefore, of main interest to develop a further understanding of the oxidation mechanisms in the investigated alloys. However, as the alloys show either excellent oxidation resistance, being accompanied with very thin oxide scales (eutectic reference alloy and alloy A), or pesting behaviour (eutectoid reference alloy and alloy B), a systematic assessment of differences and similarities among the entire alloy series is not possible for this temperature. Therefore, the following analysis strategy is applied to the results obtained at 1200 °C and for 100 h of cyclic oxidation. Although, 1200 °C are selected, it is assumed that the results can be transferred to lower temperatures. This assumption is mainly based on the different nature of the present oxidation processes.

It is still questionable whether the forming oxide scales are passivating or if the evaporation of MoO_3 is dominating, as the experimentally determined weight change m^{exp} represents the balance of mass gain m_O^{scale} due to oxide scale growth by incorporation of O and mass loss m_{Mo}^{vapour} due to evaporation of Mo in form of MoO_3:

$$\frac{m^{exp}}{A} = \frac{m_O^{scale}}{A} + \frac{m_{Mo}^{vapour}}{A} \quad (1)$$

$$\text{with } \frac{m_O^{scale}}{A} \geq 0 \text{ and } \frac{m_{Mo}^{vapour}}{A} \leq 0.$$

Nevertheless, the detailed mock-up of the formed scales is known by the previously shown microstructural investigations in Fig. 8: the thicknesses of the sublayers (d^{top} for the top TiO_2 layer,

d^{duplex} for the duplex layer) and volume fractions of the formed oxides are known ($v_{SiO_2}^{duplex}$ and $v_{TiO_2}^{duplex}$). This permits to calculate m_O^{scale} and deduce m_{Mo}^{vapour} from Eq. (1). Therefore, several assumptions are made: (i) the internal oxidation is at first neglected (However, it is not considered to be negligible as its impact is increasing in the alloys with decreasing nominal Ti content. Therefore, the changes by considering internal oxidation are qualitatively assessed at the end of the Section), (ii) the TiO_2 top layer is growing outward and (iii) the SiO_2-TiO_2 duplex scale inward (as has been proven in a three-phase Mo-Si-B-Ti alloy system by Azim et al. in Ref. [6]). The resulting mass loss at 1200 °C after 100 h due to evaporation m_{Mo}^{vapour} is in the order of (-7 ± 2) mg/cm^2 (eutectic), (-10 ± 2) mg/cm^2 (alloy A), (-16 ± 5) mg/cm^2 (alloy B) and (-27 ± 4) mg/cm^2 (eutectoid). Please note that experimental mass change and microstructural data (thicknesses and volume fractions) of one and the same sample were used in the calculation for each mass loss. The error bars represent a conservative estimate of the limits of the method by considering the standard deviations of the measured oxide scale thicknesses. Details of the calculation are provided in the Appendix. The varying impacts of the molar masses need to be considered, as the evaporating Mo possesses a significantly higher molar mass compared to incorporated O. Therefore, the respective amounts of n_{Mo}^{vapour}, n_{Si}^{scale} and n_{Ti}^{scale} are calculated. The according formulas for these quantities are also appended to this article (see Appendix).

The results are summarised in Fig. 10. The upper bar chart displays the evolution of the amount of reacting, metallic species for the entire alloy series. It is revealed that the amount of Si being oxidised is almost constant, while the amount of Ti is slightly increasing. In contrast, the amount of Mo being evaporated is significantly increasing. When taking the ratio of the oxidised Si and Ti atoms and the evaporated Mo atoms into account (lower bar chart), it can be concluded that the extent of solid oxide scale growth of the investigated alloys is comparable, but the evaporation is gaining dominance with decreasing nominal Ti content. Moreover, the corresponding ratios of the nominal chemical composition in the alloys are within 2.7 (eutectic) and 1.2 (eutectoid). These ratios correlate well with the observed trend but are significantly lower than the ratio observed for the oxidation processes. Ti and Si are significantly more consumed during oxidation as provided by the substrate in the eutectic alloy and alloy A. This difference is much smaller for alloy B and the eutectoid alloy. It is suggested that the MoO_3 evaporation is more pronounced in Mo-rich alloys, especially in alloy B and the eutectoid alloy, due to probable less passivating character of the formed oxide scales. Moreover, the calculation resembles a conservative approach. If the internal oxidation would have been considered, then the absolute value of m_{Mo}^{vapour} would be reduced, as the amount of oxygen uptake would be increased while the experimental mass change would be the same (see Eq. (1)), and the drawn conclusions might be even more shifted towards an intense scale formation. When taking the variations of the experimentally determined mass changes with time of both reference alloys into account, it is obvious that different characteristics are exhibited. In the eutectic reference alloy, the mass changes stabilise after 50 h and it seems that the oxide scale growth is dominant. In contrast, in the eutectoid reference alloy the mass

changes are still declining after 100 h highlighting the significance of ongoing evaporation. Conclusively, the oxide scales forming on the eutectic alloy are regarded as passivating, whereas on the eutectoid alloy they do not seem to be entirely dense and, therefore, enabling further evaporation.

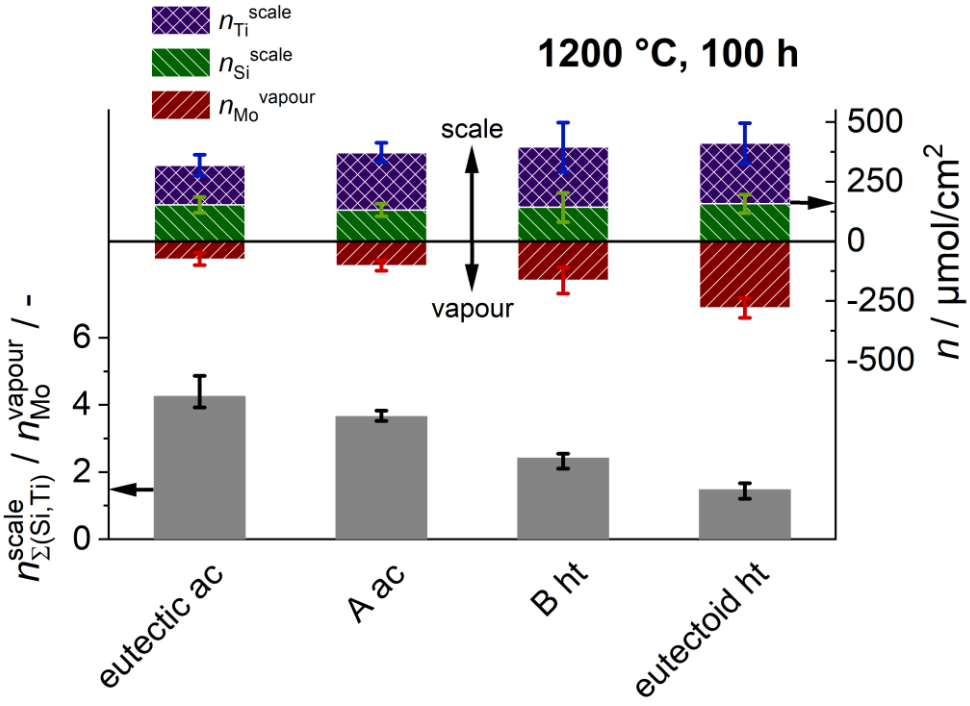

Fig. 10 Calculated amounts of oxidised Ti and Si; and Mo being evaporated at 1200 °C after 100 h in the investigated alloys and the corresponding ratio of the solid oxidised species Ti and Si; and evaporated Mo.

3.3. Creep behaviour

As alloy A shows satisfactory oxidation resistance between 800 and 1200 °C, it was subjected to compressive creep testing in order to verify that a successful combination of oxidation and creep resistance was achieved. Fig. 11a shows the true compressive creep rate as a function of true strain at 1200 °C and at stresses ranging from 50 to 300 MPa. The evolution of strain rate in dependence of true strain is characterised by minimum creep rates, which are highlighted by square markers. This applies to both reference alloys, the eutectic and the eutectoid as well; as previously shown in Ref. [8]. The minimum creep rates are attained in alloy A after 1 – 2.5 % true strain after a significant drop in creep rate during the primary creep stage has been observed. While the true strain attained at the creep rate minimum is increasing with decreasing true stress in the range of 100 – 300 MPa, there seems to be a change in creep mechanism at 50 MPa as a slight decrease in true strain is observed compared to 100 MPa. A change in creep mechanism is further indicated by the less pronounced transient creep rate drop at 50 MPa. Diffusional creep seems to become more relevant due to sufficient duration of loading.

Minimum true creep rates in dependence of the true compressive stress are summarised in the double-logarithmic Norton plot shown in Fig. 11b and compared to the eutectic and eutectoid reference alloys and the corresponding monolithic phases. Alloy A exhibits an intermediate creep resistance in comparison to the eutectic and eutectoid alloys. By comparing the creep resistance of the monolithic phases Ti_5Si_3, Mo_5Si_3 and single-phase $(Mo,Si,B)_{SS}$, it is obvious that these frame the creep behaviour

of all investigated alloys. Thereby, the creep resistance of the eutectic and eutectoid reference alloys is dominated by the less creep resistant phase $(Ti,Mo)_5Si_3$ and the improved creep resistant phase $(Mo,Ti)_5Si_3$, respectively.

The stress exponent n of the power law for $\dot{\varepsilon}_{min}$:

$$\dot{\varepsilon}_{min} \propto \sigma^n \tag{2}$$

was determined to be 3.5 in alloy A, revealing similar creep characteristics as the eutectic and eutectoid reference alloys which exhibit stress exponents of 3.7 and 3.5, respectively [8]. This indicates that creep is dislocation climb controlled throughout the alloy series as was also found by Schliephake et al. in the former developed three phase Mo-Si-B-Ti alloys (Mo_{SS} + $(Ti,Mo)_5Si_3$ + Mo_5SiB_2) [7].

The apparent activation energy of creep Q_c in alloy A based on the Arrhenius term for $\dot{\varepsilon}_{min}$:

$$\dot{\varepsilon}_{min} \propto e^{-\frac{Q_c}{RT}} \tag{3}$$

was determined at a true stress of 200 MPa and was found to be 484 kJ/mol (see Suppl. 6). In comparison, the activation energies in the eutectic and eutectoid reference alloys were determined to be 471 kJ/mol and 444 kJ/mol supporting above statement of similar creep characteristics [8]. As the apparent activation energies of both reference alloys and alloy A are in the same order and similar/same creep mechanism are active in all alloys, the minimum true creep rate at a specific, absolute temperature can be normalised to the solidus temperature and plotted in an Arrhenius plot as shown in Fig. 11c. This plot utilising inverse homologous temperatures finally leads to a single master straight for all investigated alloys. This proves that the observed difference in creep resistance at 1200 °C is caused by the different applied homologous temperatures. Conclusively, the argumentation of the increased creep resistance of the eutectoid alloy and of the eutectoid region in the intermediate alloys in general, cannot be based solely on the presence of $(Mo,Ti)_5Si_3$. This is further confirmed by an additional compression creep test of alloy A at an increased temperature of 1318 °C which is equivalent to the homologous temperature of 0.74 at which the eutectic reference alloy has been compression creep tested. This compression creep test was conducted at 100 MPa and is highlighted with a bright red diamond marker in Fig. 11b. Both, the intermediate alloy A and the eutectic reference alloy exhibit comparable creep resistance when the tests were performed at identical homologous temperature.

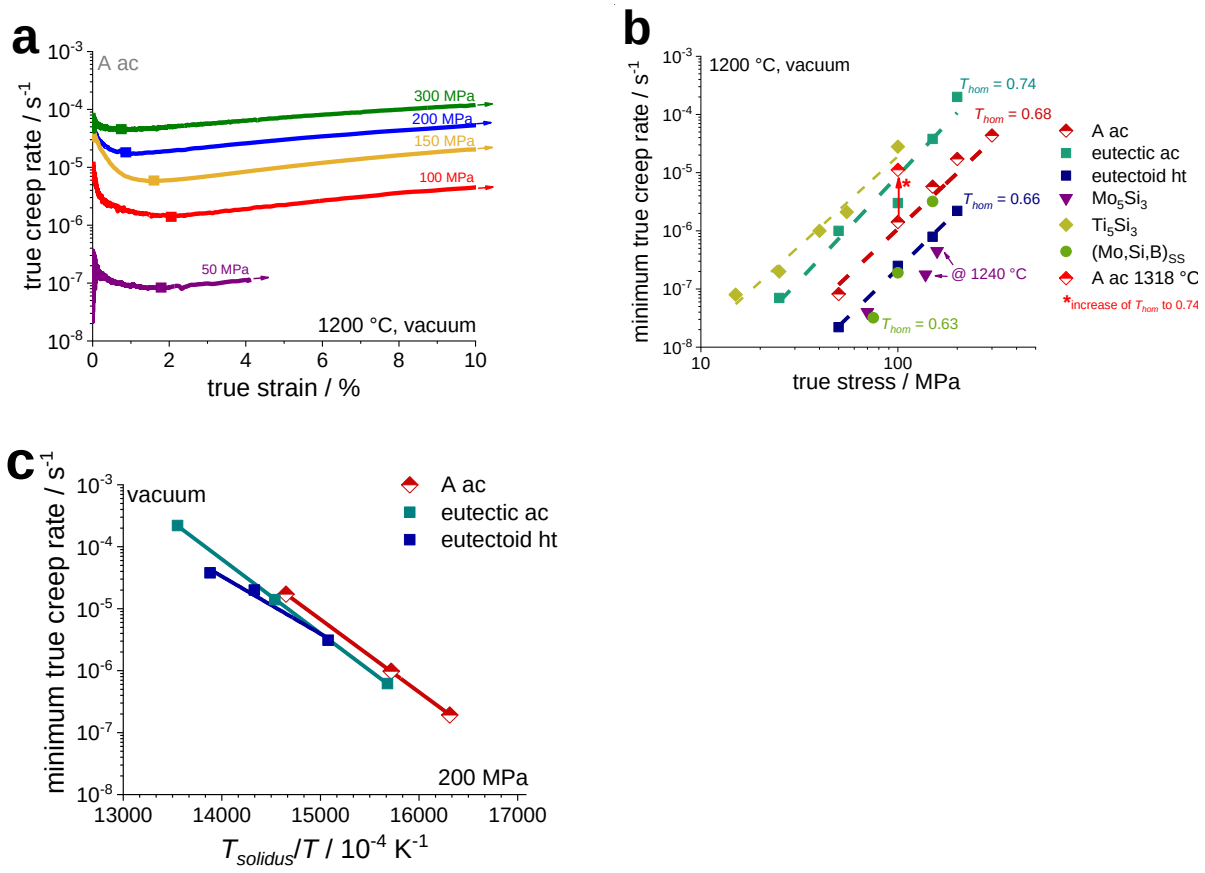

Fig. 11 Compressive true stress curves of alloy A (a), the corresponding Norton plot with literature data for comparison [3, 8, 21, 22] (b) and Arrhenius plot utilising inverse homologous temperature for alloy A and the reference alloys (c).

4. Summary and Conclusion

Novel, fine-structured Mo-Si-Ti alloys with tailored eutectic-eutectoid microstructure were successfully developed in this paper, namely a Ti-rich alloy A and a Ti-lean alloy B. Amongst all alloys, including the eutectic and eutectoid reference alloys, it was found that, in addition to the eutectic reference alloy [8], pesting could be suppressed at 800 °C in the novel alloy A. This was attributed to a threshold in nominal Ti content of minimum 43 at% and average Ti content in Mo_{SS} lamellae in eutectic and eutectoid regions of minimum 35 at%, respectively, combined with at least 50 vol% eutectic regions which presumably balance the pesting nature of the eutectoid. At higher temperatures of 1100 and 1200 °C all investigated alloys revealed a top TiO_2 layer with an underlying TiO_2-SiO_2 duplex scale providing suitable oxidation resistance. The duplex scale seems to be essential to guarantee adequate oxidation resistance, as sole TiO_2 is believed to be non-protective due to its high diffusion coefficient for O [23] and its proneness to cracking [24]. Most recent thermodynamic evaluations of the SiO_2-TiO_2 phase diagram [25] and studies on the solubility of SiO_2 in rutile TiO_2 with varying pressures [26] propose that there is no solubility between the respective oxides at atmospheric pressure and ambient temperatures to about 1550 °C. It has been reported that additions of Si below 1 wt% Si in Ti-Si alloys lead to a significant enhancement of the oxidation resistance due to a change in morphology of the top TiO_2 layer improving the oxide scale adherence and preventing stratification [27]. These authors suggested that Si in TiO_2 has an influence on the O vacancies which might lead to deceleration of the

diffusion rate of O in TiO_2 [27]. Conclusively, it is assumed that the presence of Si/SiO_2 in TiO_2 might reduce the mobility of O and thereby improving its oxidation behaviour. The volume fractions and network structure of the respective oxides in the duplex scale were analysed after 100 h at 1200 °C in order to determine the matrix forming oxide. The performed cluster analysis confirmed a mixed SiO_2-TiO_2 matrix character among all tested alloys, including the eutectic and eutectoid reference alloys. Especially, penetrating TiO_2 pathways were observed in all alloys. This reveals that an adequate oxidation resistance is achieved even without a continuous SiO_2 matrix. As the oxidation behaviour is characterised by the superposition of mass gain due to solid oxide growth and mass loss caused by evaporation of MoO_3, the individual contributions were analysed at 1200 °C after 100 h highlighting the dominant oxidation mechanism. It was found that evaporation of MoO_3 gains significance with decreasing nominal Ti content. In the eutectic alloy, solid oxide growth predominates the oxidation behaviour leading to the assumption that the forming oxide scale is passivating. These observations might be transferred to lower temperatures explaining the outstanding oxidation behaviour of the eutectic alloy at 800 °C. Moreover, the adequate oxidation resistance of the intermediate eutectic-eutectoid alloy A in the temperature regime of 800 to 1200 °C could be successfully combined with satisfactory compressive creep resistance. At 1200 °C, alloy A possesses lower minimum creep rates than the eutectic reference alloy while exhibiting the same creep mechanism. However, the apparent difference in creep resistance was mainly caused by the different solidus temperatures of the alloys and, thus, different applied homologous temperatures.

Acknowledgements

The authors gratefully acknowledge financial support by Deutsche Forschungsgemeinschaft (DFG) within the framework of grants no. HE 1872/33-1. Many thanks are additionally given to the collaboration partners Ronja Anton, Nadine Laska and Uwe Schulz from the Institute of Materials Research, German Aerospace Center (DLR), and Matthias Weber, Bronislava Gorr and Hans-Jürgen Christ from the Institute for Materials Engineering, University of Siegen. Additionally, the authors would like to thank Lara Alavi for several oxidation tests.

Appendix

As already described, the observed specific mass changes are resulting from two contributions:

$$\frac{m^{exp}}{A} = \frac{m_O^{scale}}{A} + \frac{m_{Mo}^{vapour}}{A} \qquad \text{(App. 1)}$$

$$\text{with } \frac{m_O^{scale}}{A} \geq 0 \text{ and } \frac{m_{Mo}^{vapour}}{A} \leq 0$$

For the sake of clarity, A is omitted in the following because it is not changing significantly during oxidation. In the detail, the contributions to mass gain by scale growth can be itemized as follows:

$$m_O^{scale} = m_O^{duplex} + m_O^{top} + m_O^{internal}$$

$$= m_{O\ in\ TiO_2}^{duplex} + m_{O\ in\ SiO_2}^{duplex} + m_{O\ in\ TiO_2}^{top} + m_O^{internal} \quad \text{(App. 2)}$$

The contribution by internal oxidation is neglected for now: $m_O^{internal} = 0$. By using $m_{O\ in\ TiO_2} = 2\ n_{TiO_2}\ M_O$ and $m_{O\ in\ SiO_2} = 2\ n_{SiO_2}\ M_O$, (App. 3) is obtained:

$$m_O^{scale} = 2\ n_{TiO_2}^{duplex}\ M_O + 2\ n_{SiO_2}^{duplex}\ M_O + 2\ n_{TiO_2}^{top} M_O \quad \text{(App. 3)}$$

When applying $n = {}^{m}/_{M}$ and $m = \rho\ V$, this transforms into:

$$m_O^{scale} = 2\ M_O \left(\frac{\rho_{TiO_2}\ V_{TiO_2}^{duplex}}{M_{TiO_2}} + \frac{\rho_{SiO_2}\ V_{SiO_2}^{duplex}}{M_{SiO_2}} + \frac{\rho_{TiO_2}\ V^{top}}{M_{TiO_2}} \right) \quad \text{(App. 4)}$$

The top layer is homogenous and its volume V^{top} is directly calculated from its thickness on the cuboid shape sample. The duplex layer is inhomogeneous and the respective volume fractions of the oxide phases as shown in Fig. 8 are utilized to calculate the respective volumes $V_{TiO_2}^{duplex} = v_{TiO_2}^{duplex}\ V^{duplex}$ and $V_{SiO_2}^{duplex} = v_{SiO_2}^{duplex}\ V^{duplex}$. The calculations shown in this article consider that the duplex layer is growing inward [6].

$$m_O^{scale} = 2\ M_O \left[V^{duplex} \left(\frac{\rho_{TiO_2}\ v_{TiO_2}^{duplex}}{M_{TiO_2}} + \frac{\rho_{SiO_2}\ v_{SiO_2}^{duplex}}{M_{SiO_2}} \right) + V^{top}\ \frac{\rho_{TiO_2}}{M_{TiO_2}} \right] \quad \text{(App. 5)}$$

Hence,

$$m_{Mo}^{vapour} = m^{exp} - m_O^{scale} \quad \text{(App. 6)}$$

By applying $n = {}^{m}/_{M}$, the amounts of metallic species consumed in the oxidation processes can be calculated:

$$n_{Mo}^{vapour} = \frac{m_{Mo}^{vapour}}{M_{Mo}} \quad \text{(App. 7)}$$

$$n_{Si}^{scale} = n_{Si}^{duplex} = n_{SiO_2}^{duplex} = \frac{m_{SiO_2}^{duplex}}{M_{SiO_2}}$$

$$= \frac{\rho_{SiO_2}\ V_{SiO_2}^{duplex}}{M_{SiO_2}} = \frac{\rho_{SiO_2}}{M_{SiO_2}}\ v_{SiO_2}^{duplex}\ V^{duplex} \quad \text{(App. 8)}$$

$$n_{Ti}^{scale} = n_{Ti}^{duplex} + n_{Ti}^{top} = n_{TiO_2}^{duplex} + n_{TiO_2}^{top}$$

$$= \frac{m_{TiO_2}^{duplex} + m_{TiO_2}^{top}}{M_{TiO_2}} = \frac{\rho_{TiO_2}}{M_{TiO_2}} \left(v_{TiO_2}^{duplex}\ V^{duplex} + V^{top} \right) \quad \text{(App. 9)}$$

Finally, the observed ratio of amounts of Si and Ti in the oxide scales to evaporating Mo is analysed: ${n_{\Sigma(Si,Ti)}^{scale}}/{n_{Mo}^{vapour}}$. The at first neglected internal oxidation further increases the obtained ratios. Increasing ratios indicate faster growth rates of the solid scales than evaporation rates which is in keeping with the observed oxidation stability at 1200 °C.

References

1. D. M. Berczik, Method for enhancing the oxidation resistance of a molybdenum alloy, and a method making a molybdenum alloy. 1997.
2. D. M. Berczik, Oxidation resistant molybdenum alloy. 1997.
3. P. Jain, K. S. Kumar, Tensile creep of Mo–Si–B alloys. Acta Materialia, 2010. 58(6): p. 2124-2142.
4. T. A. Parthasarathy, M. G. Mendiratta, D. M. Dimiduk, Oxidation mechanisms in Mo-reinforced Mo5SiB2 (T2)–Mo3Si alloys. Acta Materialia, 2002. 50(7): p. 1857-1868.
5. D. M. Dimiduk, J. H. Perepezko, Mo-Si-B alloys: developing a revolutionary turbine-engine material. MRS Bulletin, 2003. 28(9): p. 639-645.
6. M. A. Azim, S. Burk, B. Gorr, H.-J. Christ, D. Schliephake, M. Heilmaier, R. Bornemann, P. H. Bolívar, Effect of Ti (Macro-) Alloying on the High-Temperature Oxidation Behavior of Ternary Mo–Si–B Alloys at 820–1300° C. Oxidation of Metals, 2013. 80(3-4): p. 231-242.
7. D. Schliephake, M. A. Azim, K. v. Klinski-Wetzel, B. Gorr, H.-J. Christ, H. Bei, E. P. George, M. Heilmaier, High-Temperature Creep and Oxidation Behavior of Mo-Si-B alloys with High Ti Contents. Metallurgical and Materials Transactions A, 2014. 45(3): p. 1102-1111.
8. D. Schliephake, A. Kauffmann, X. Cong, C. Gombola, M. A. Azim, B. Gorr, H.-J. Christ, M. Heilmaier, Constitution, oxidation and creep of eutectic and eutectoid Mo-Si-Ti alloys. Intermetallics, 2019. 104: p. 133-142.
9. M. K. Meyer, A. J. Thom, M. Akinc, Oxide scale formation and isothermal oxidation behavior of Mo–Si–B intermetallics at 600–1000 C. Intermetallics, 1999. 7(2): p. 153-162.
10. S. Paswan, R. Mitra, S. K. Roy, Oxidation behaviour of the Mo–Si–B and Mo–Si–B–Al alloys in the temperature range of 700–1300°C. Intermetallics, 2007. 15(9): p. 1217-1227.
11. F. A. Rioult, S. D. Imhoff, R. Sakidja, J. H. Perepezko, Transient oxidation of Mo–Si–B alloys: effect of the microstructure size scale. Acta Materialia, 2009. 57(15): p. 4600-4613.
12. V. Supatarawanich, D. R. Johnson, C. C. T. Liu, Effects of microstructure on the oxidation behavior of multiphase Mo–Si–B alloys. Materials Science and Engineering A, 2003. 344(1-2): p. 328-339.
13. J. B. Nelson, D. P. Riley, An experimental investigation of extrapolation methods in the derivation of accurate unit-cell dimensions of crystals. Proceedings of the Physical Society, 1945. 57(3): p. 160-177.
14. B. Pedel, Mo-Ti (Molybdenum-Titanium), in Li-Mg–Nd-Zr. Zrandolt-Börnstein - Group IV Physical Chemistry, M. O., Editor. 1997, Springer: Berlin, Heidelberg. p. 1-3.
15. D. Sturm, M. Heilmaier, J. H. Schneibel, P. Jéhanno, B. Skrotzki, H. Saage, The influence of silicon on the strength and fracture toughness of molybdenum. Materials Science and Engineering: A, 2007. 463(1-2): p. 107-114.
16. S. Majumdar, B. Gorr, H.-J. Christ, D. Schliephake, M. Heilmaier, Oxidation mechanisms of lanthanum-alloyed Mo-Si-B. Corrosion Science, 2014. 88: p. 360-371.
17. J. J. Williams, M. Akinc, Oxidation Resistance of Ti_5Si_3 and $Ti_5Si_3Z_x$ at 1000° C (Z= C, N, or O). Oxidation of Metals, 2002. 58(1-2): p. 57-71.
18. M. A. Azim, B. Gorr, H.-J. Christ, O. Lenchuk, K. Albe, D. Schliephake, M. Heilmaier, Effect of Ti content and nitrogen on the high-temperature oxidation behavior of $(Mo, Ti)_5Si_3$. Intermetallics, 2017. 90: p. 103-112.
19. S. Burk, B. Gorr, H.-J. Christ, D. Schliephake, M. Heilmaier, C. Hochmuth, U. Glatzel, High-temperature oxidation behaviour of a single-phase $(Mo, Ti)_5Si_3$ (Mo–Si–Ti) alloy. Scripta Materialia, 2012. 66(5): p. 223-226.
20. M. A. Azim, D. Schliephake, C. Hochmuth, B. Gorr, H.-J. Christ, U. Glatzel, M. Heilmaier, Creep Resistance and Oxidation Behavior of Novel Mo-Si-B-Ti Alloys. JOM, 2015. 67(11): p. 2621-2628.
21. M. K. Meyer, M. Akinc, Oxidation Behavior of Boron-Modified Mo_5Si_3 at 800°–1300°C. Journal of the American Ceramic Society, 1996. 79(4): p. 938-944.
22. K. Sadananda, C. R. Feng, R. Mitra, S. C. Deevi, Creep and fatigue properties of high temperature silicides and their composites. Materials Science and Engineering A, 1999. 261(1-2): p. 223-238.

23. J. Unnam, R. N. Shenoy, R. K. Clark, Oxidation of commercial purity titanium. Oxidation of Metals, 1986. 26(3-4): p. 231-252.
24. J. E. L. Gomes, A. M. Huntz, Comparison of the kinetics and morphologic properties of titanium, Ti-1.5 Ni and Ti-2.5 Cu during oxidation in pure oxygen between 600 and 820° C. Oxidation of Metals, 1980. 14(6): p. 471-498.
25. S. A. Kirillova, V. I. Almjashev, V. V. Gusarov, Phase relationships in the SiO_2-TiO_2 system. Russian Journal of Inorganic Chemistry, 2011. 56(9): p. 1464-1471.
26. Y. Ren, Y. Fei, J. Yang, W. Bai, SiO_2 solubility in rutile at high temperature and high pressure. Journal of Earth Science, 2009. 20(2): p. 274-283.
27. A. M. Chaze, C. Coddet, Influence of silicon on the oxidation of titanium between 550 and 700°C. Oxidation of metals, 1987. 27(1-2): p. 1-20.

Supplementary:

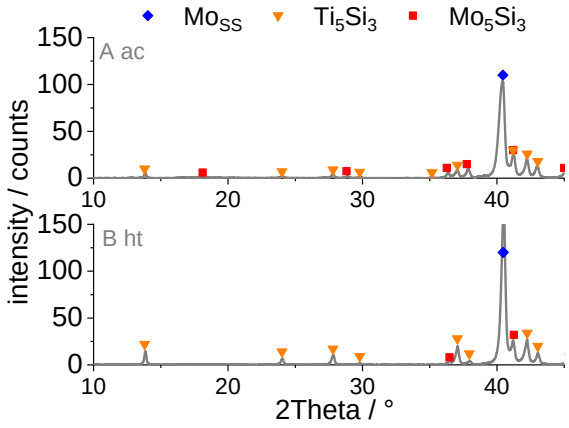

Suppl. 1 XRD diffraction patterns revealing evidence for the present phases in the as-cast state of alloy A and the heat-treated state of alloy B.

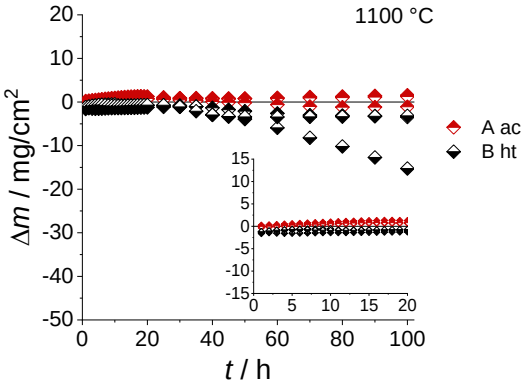

Suppl. 2 Specific weight change as a function of time during cyclic oxidation for the investigated alloys A and B at 1100 °C.

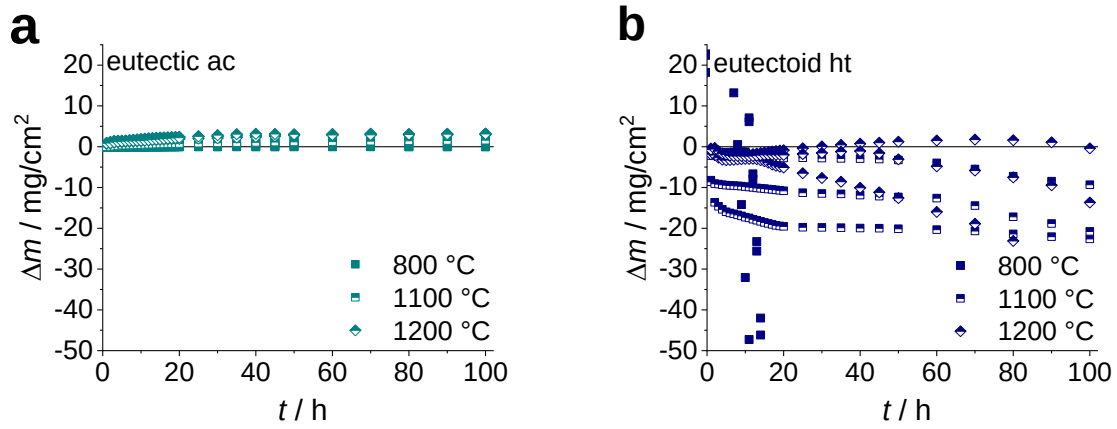

Suppl. 3 Specific weight change as a function of time during cyclic oxidation for the eutectic (a) and eutectoid (b) alloy.

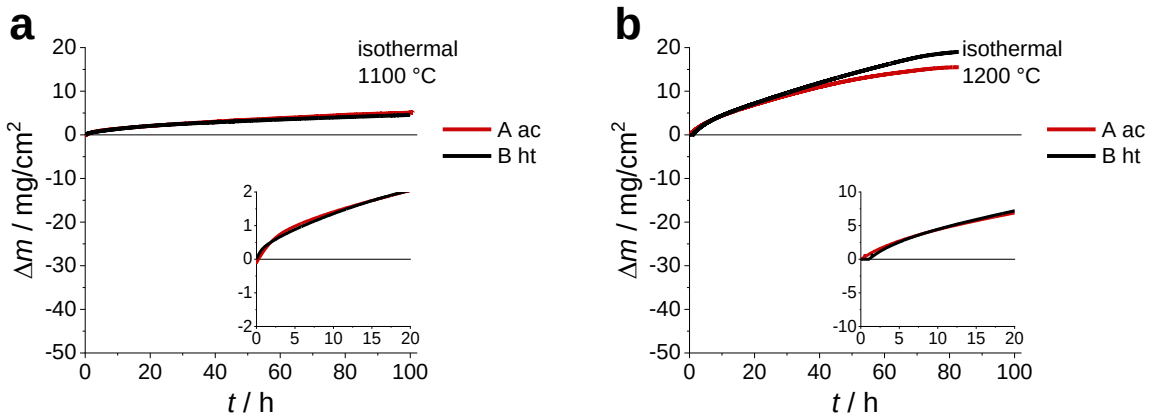

Suppl. 4 Specific isothermal weight change of alloys A and B as a function of exposure time at 1100 °C (a) and 1200 °C (b).

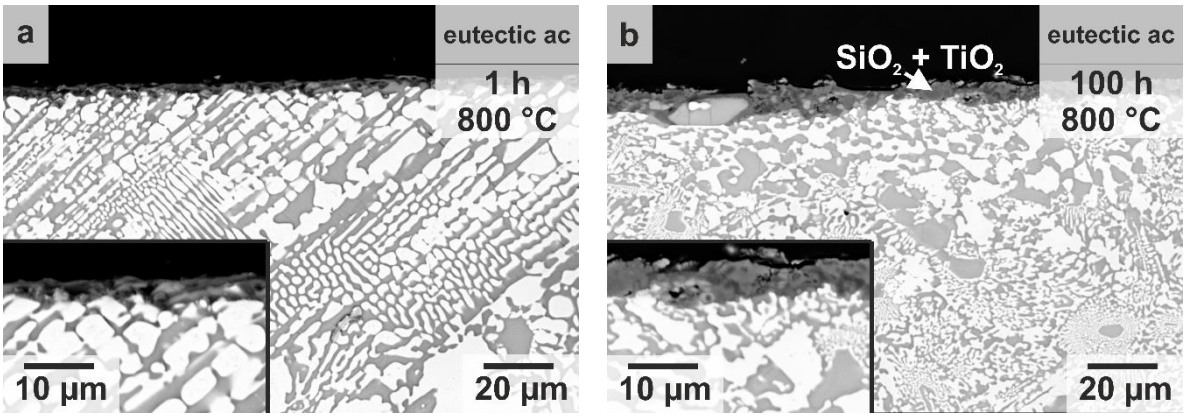

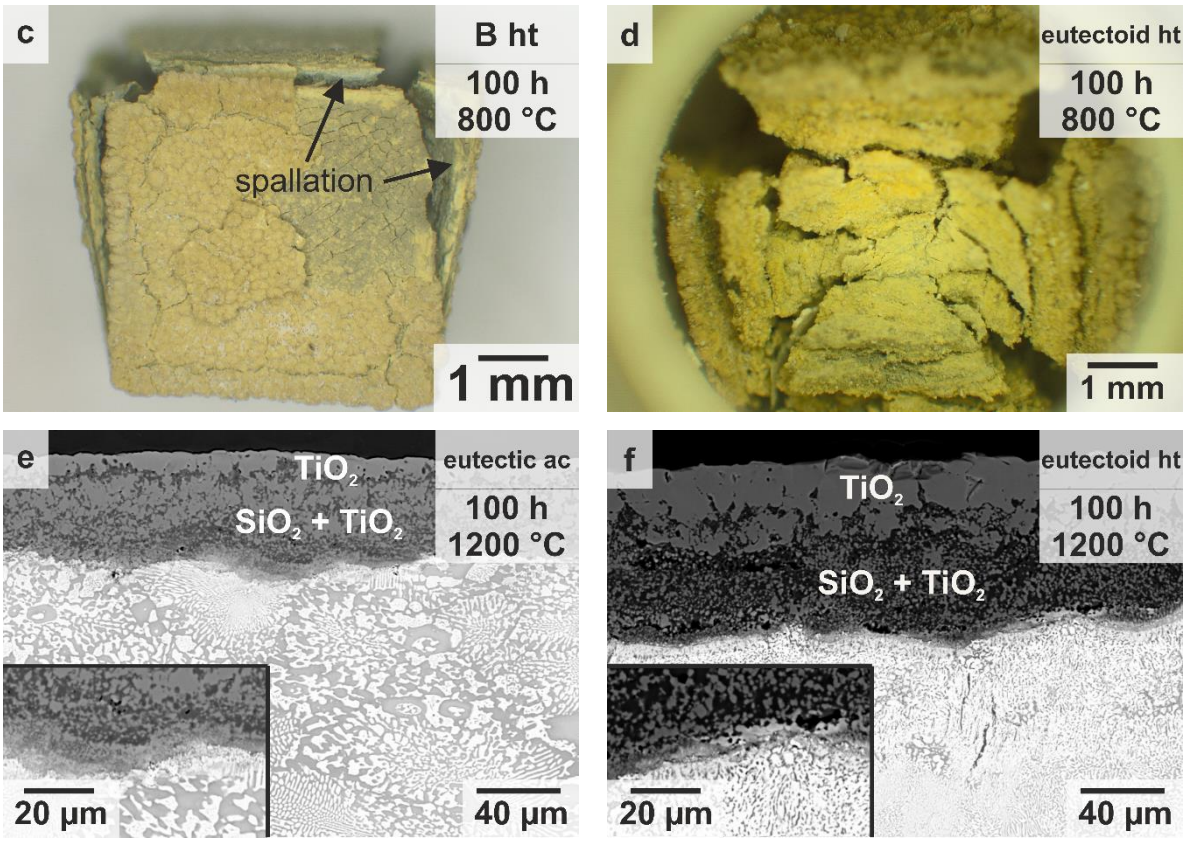

Suppl. 5 BSE micrograph of the eutectic reference alloy cyclically oxidised at 800 °C after 1h (a) and 100 h (b). Overall images of alloy B (c) and of the eutectoid reference alloy (d) after cyclic oxidation at 800 °C after 100 h. BSE micrographs of oxidised samples at 1200 °C after 100 h of the eutectic (e) and eutectoid (f) alloy.

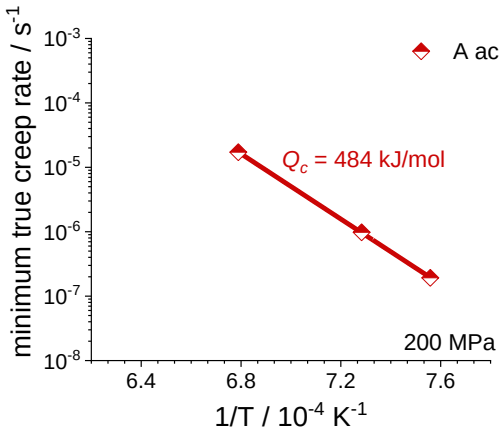

Suppl. 6 Respective Arrhenius plot for activation energy determination in alloy A.